Ultra-Wide-Swath SAR Imaging Enabled by Multiple-Elevation-Beam F-Scan With Two-Burst ScanSAR

João Pedro Turchetti Ribeiro, *Graduate Student Member, IEEE*, Thomas Kraus, Markus Bachmann, Gerhard Krieger, *Fellow, IEEE*, and Alberto Moreira, *Fellow, IEEE*

***Abstract*—This article presents a comprehensive study of a novel synthetic aperture radar (SAR) technique designed for ultra-wide-swath imaging with high azimuth resolution. It provides a thorough explanation of the concept, design, and performance prediction of the proposed mode. The unambiguous imaging of the wide swath is enabled by using frequency scanning (F-Scan) with multiple simultaneous elevation beams. The resulting blind ranges are solved by employing a two-burst ScanSAR approach. The key guiding design principle is to achieve homogeneous performance across the scene, without prioritizing one direction or region over the others. For this purpose, the main techniques applied are the processing of a variable power beamwidth (PBW), the use of nonlinear chirps, and the transmission of subpulses. These methods ensure an equalized ground range resolution and noise-equivalent sigma-zero (NESZ) in range. The novel mode is shown to achieve both ultra-wide swaths up to 500 km, high azimuth resolution, and also very high image quality.**

***Index Terms*—Frequency scanning (F-Scan), multiple elevation beams, ScanSAR, synthetic aperture radar (SAR), ultra-wide swath.**

I. INTRODUCTION

SYNTHETIC aperture radar (SAR) imaging at large scales is essential for advancing remote sensing applications across diverse fields, such as environmental and climate monitoring, disaster management, and defense. Unlike optical imaging, SAR operates in all weather conditions, providing consistent, high-resolution data regardless of cloud cover or sunlight [1].

The current state of SAR systems allows for the imaging of either vast regions with coarse resolution or small areas with very high resolution. For instance, in X-band, current systems are capable of imaging small patches of 5 km with submeter resolution by employing spotlight modes. The coverage can be strongly improved to swaths of 100 km by using the ScanSAR mode, but at the expense of a coarser azimuth resolution of around 20 m [2], [3], [4], [5]. The HRWS mission proposal would further enhance the swath width to 500 km at an azimuth resolution of 16 m by employing digital beamforming (DBF) in azimuth [6], [7]. The current state of the art is Sentinel-1, which acquires swaths of 250 km with an azimuth resolution of 20 m in C-band [8]. Its follow-up mission, Sentinel-1 Next Generation, is planned to increase the swath width to 400 km and improve the resolution to 5 m by means of DBF in range and azimuth [9].

The natural trend for future missions is to achieve such ultra-wide swaths at an ever finer resolution, thus allowing the fast coverage of large regions of the Earth with high resolution. For this purpose, advanced techniques to overcome this well-known tradeoff between coverage and resolution have been published in the literature. These techniques are based mainly on multichannel approaches, both in azimuth and elevation.

The first developments were published by Currie and Brown [10] by taking advantage of the inherent versatility of phased-array antennas and the use of multiple channels. For instance, they suggested using multiple elevation beams to cover different subswaths to increase the coverage. Similarly, in azimuth, the technique commonly known as the displaced phase center antenna (DPCA) was proposed. It consists in transmitting with a wide azimuth beam and receiving through multiple channels displaced in azimuth to increase the effective sampling, thereby allowing for enhanced azimuth resolution.

Further developments of these techniques were brought up by Suess et al. [11] and Suess and Wiesback [12], who suggested using separate transmit and receive antennas, allowing for the optimization of the RF design. The system proposed consists of a small broad-beam transmit antenna with high power and low losses enabled by the use of traveling wave tubes, and a dedicated multichannel antenna on receive, applying what is today known as DBF both in azimuth and in elevation.

The DPCA technique previously required that the platform moves exactly half the antenna length between consecutive receive events, to ensure a uniform sampling along azimuth. In 2004, a reconstruction technique for the nonuniform sampling case was first introduced in [13]. Krieger et al. [14], [15], [16] also published a comprehensive investigation of high-resolution wide-swath imaging techniques for a monostatic system, in which the wide transmit beams are obtained by amplitude and phase tapering. It was also proposed to use multiple waveforms together with dividing the transmit pulse

Received 26 May 2025; revised 24 November 2025; accepted 4 January 2026. Date of publication 26 January 2026; date of current version 17 February 2026. *(Corresponding author: João Pedro Turchetti Ribeiro.)*

The authors are with the Microwaves and Radar Institute, German Aerospace Center (DLR), 82234 Weßling, Germany (e-mail: joao.turchettiribeiro@dlr.de).

Digital Object Identifier 10.1109/TGRS.2026.3657888

into subpulses, which would be separated by means of DBF on receive.

The use of DBF on receive in elevation (generation of multiple elevation beams) has been widely suggested in the literature to spatially filter the otherwise ambiguous echoes of wide swaths. This technique is commonly known as SCan-On-REceive (SCORE) and is typically combined with pulse repetition interval (PRI) variation approaches to overcome the blind ranges [17], [18], [19], [20]. Although very promising, this technique is, nevertheless, still complex and hard to realize within restricted budgetary constraints [6]. More interestingly for this research, in [14], the concept of a continuous intrapulse beamsteering in elevation was introduced, i.e., transmitting first to far range and scanning toward near range. This approach leads to benefits in terms of shorter receive echo windows, wider swaths, and more homogeneous signal-to-noise ratio (SNR) performance across wide swaths.

A relatively simple implementation of such a continuous beamsteering was proposed by Roemer [21], [22] in 2017 through a technique known as frequency scanning (F-Scan). The idea behind F-Scan is to employ a pencil-beam antenna in elevation whose pointing varies as a function of the frequency. This scan from far to near range is achieved with the sole use of phase shifters (PSs) and true-time-delay lines. Such an analog beamsteering, when compared to DBF implementations, has the benefits of much lower hardware complexity and costs. Moreover, the use of a pencil beam both on transmit and on receive leads to improvements in SNR. The drawback is the distribution of the total transmit bandwidth across the scene, thus reducing the range resolution. The new International Telecommunication Union (ITU) allocation of 1200 MHz in X-band allows, however, for some compensation of this resolution loss.

F-Scan has been further investigated in several other publications. In 2020, the signal modeling and processing with focus on range ambiguity reduction was published in [23]. Two years later, comprehensive descriptions of the mode and instrument parameters for the design of F-Scan acquisitions were derived in [24] and [25]. Quantization methods for efficient data volume reductions of F-Scan acquisitions were described in [26]. The possibilities of equalizing the ground range resolution and obtaining adaptive SNR were first introduced in [24] and then further developed in [27]. This would be achieved using a tailored time- and frequency-dependent beam steering. Unfortunately, the frequency dependence is described as not yet feasible with the current stage of technology.

This article at hand presents a comprehensive investigation of a novel imaging technique to achieve ultra-wide swaths and very high image quality. The mode consists in transmitting with F-Scan to a very wide swath, wider than the unambiguous range dictated by the pulse repetition frequency (PRF). Therefore, the echoes relative to each transmit pulse are received in multiple consecutive echo windows. The echoes are filtered in the space–frequency domain with the analog beamsteering of F-Scan. The resulting blind ranges are overcome with a two-burst ScanSAR approach. This technique is currently patent pending [28] and has already been briefly introduced in [29].

This article is structured as follows. In Section II, the imaging mode concept is initially presented, followed by the detailing of the basic techniques and the optimization approaches. The performance estimation, mainly in terms of resolution, ambiguity levels, and noise-equivalent sigma-zero (NESZ), is described in Section III. Section IV discusses a few alternatives to the proposed mode and also ideas for future work. Finally, Section V concludes this article, summarizing the main take-away messages and the results obtained.

II. MULTIPLE-ELEVATION-BEAM F-SCAN WITH TWO-BURST SCANSAR

A. Imaging Mode Concept

The proposed imaging technique—named multiple-elevation-beam F-Scan with two-burst ScanSAR—consists in initially transmitting to a very wide swath in a scanning manner, from far to near range. This continuous beamsteering is performed by varying the frequency of the transmitted chirp and is characterized by an intrinsic nonlinear relationship between frequency and antenna pointing. The starting and ending points of the scan are defined by the desired swath width and are configured via the phase shift and time-delay values selected. As the swath is very wide, the echoes do not fit in only one receive window. Consequently, in each PRI, the echoes from multiple transmit pulses are received. This effect is commonly known as range ambiguities; however, by employing F-Scan, the echoes are filtered in the space–frequency domain by taking advantage of the dispersive antenna beam and the different frequency bands associated with these otherwise ambiguous subswaths. Unfortunately, parts of the echo are lost due to the transmit events because a spaceborne monostatic SAR system usually cannot receive while transmitting. This is due to the high transmit power that exceeds the received power by many orders of magnitude and would otherwise saturate the receiver. The gap in reception is causing blind ranges in the resulting SAR image. Conveniently, transmitting to these blind ranges is not necessary so that the transmit chirp can be subdivided into subpulses. A similar approach has been investigated in the scope of SCORE by Bordoni et al. [30], [31].

As a final SAR image with blind ranges is generally undesired, multiple techniques have been discussed in the literature to overcome this issue. In agreement with the design philosophy of a low complexity system, a two-burst ScanSAR is considered in this investigation. The idea is, in contrast to a traditional ScanSAR, to illuminate the same regions during the two bursts. Then, in order to shift the position of the blind ranges from burst to burst, slightly different PRFs are employed. The PRFs are designed in a way that there is no overlap between the blind ranges of each burst. Consequently, two images are generated—one for each burst—over the same region, but with gaps in different nonoverlapping ranges. The combination of both images allows for the formation of a contiguous image. In azimuth, the continuous repetition of these two bursts allows for the mosaicking of the images, thus also avoiding gaps. This scheme can be visualized as shown in Fig. 1. On the one hand, an advantage of this approach is

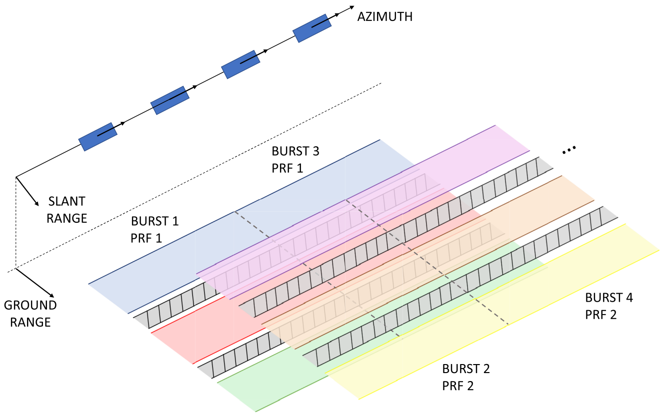

Fig. 1. Schematic of the proposed mode. The subswaths are highlighted by different colors and the blind ranges are shown in dashed gray. The overlap regions are kept to a minimum to maximize the illumination time of the imaged areas.

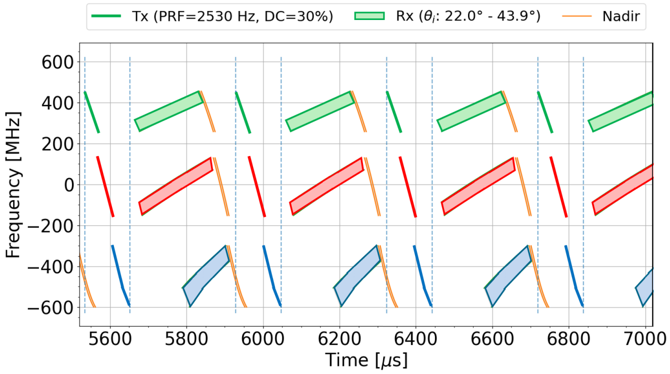

Fig. 2. Schematic time–frequency representation of the Tx and Rx events for burst 1 depicted in Fig. 1. The transmit subpulses and the echoes highlighted in green, red, and blue are related to the respective subswaths.

that it enables using high duty cycles of up to 50%. On the other hand, the azimuth resolution is deteriorated by a factor of 3 due to the sharing of the synthetic aperture.

For duty cycles lower than 50%, some regions will be imaged twice, i.e., by both bursts. The approach taken in this research is to further reduce, to the possible extent, the subpulses to ensure an overlap between the bursts of only 1 km in ground range, for mosaicking purposes. This two-step generation of subpulses—first skipping blind ranges and then reducing the overlap between the bursts—allows for longer illumination times, thus strongly improving the NESZ, as discussed in more detail in Section III-C.

A schematic of the concept is depicted in Fig. 1. The scanning beam of each subswath has been omitted for visualization purposes. The figure shows an acquisition of a 300 km wide swath ranging from 22° to 47° of incidence angle. The transmit (Tx) and receive (Rx) events of burst 1 are highlighted in the time–frequency domain in Fig. 2. The distinguishing of the echoes in the frequency domain is evident. Additionally, it can be observed that with only two bursts, six subswaths are obtained, leading to the very wide swath.

In terms of swath width, this acquisition would be equivalent to a traditional six-burst ScanSAR, but with better azimuth resolution and worse range resolution. A significant advantage of the proposed technique over traditional ScanSAR or TOPS is that in the latter, there is a significant unbalance in resolution. For instance, HRWS would achieve 2 m in range and 16 m in azimuth for the 500-km-wide ScanSAR. In this article, it will be shown that the same system can achieve 400-km swaths with a square 5 m (ground range) × 5 m (azimuth) resolution cell with the proposed technique.

TABLE I

System Parameters for the X-Band HRWS Mission

System Parameter	**Value**
Center frequency	9.8 GHz
Maximum transmit bandwidth	1200 MHz
Orbit height	519 km (LEO)
Antenna height	1.4 m (64 elements)
Antenna length	6.0 m (12 elements)
Azimuth channels (DPCA)	4
Peak transmit power	7680 W
Maximum duty cycle	30 %
Noise figure	3.7 dB
Losses	2.0 dB

Section II-B describes the system considered for generating the numerical results in this article.

B. System Description

This article introduces a technique that can be implemented in any SAR system equipped with F-Scan capabilities. For quantitative derivations, the X-band HRWS mission proposal is considered throughout this article [6], [7], [32]. The relevant system parameters are summarized in Table I.

DBF in azimuth is considered by means of the DPCA technique—also known as multiple azimuth phase centers (MAPS) [10], [13]. The technique consists essentially in splitting the antenna into multiple channels on receive, while a single transmit phase center is maintained. On transmit, the whole antenna must be used to ensure that all the transmit and receive modules (TRMs), and thus all the available power, are used. A method to generate the wide beam on transmit with phase tapering only was published in [33]. The results shown here approximate the antenna pattern on transmit to the single-channel one.

The use of DPCA poses an important constraint on the selection of the PRF. To ensure a uniform sampling in azimuth, the PRF must be such that the effective phase centers between two consecutive receive events are uniformly distributed. This is achieved, for instance, when the platform moves exactly half the antenna length between PRIs. For the system parameters considered, one obtains the uniform sampling PRF by

$$\mathrm{PRF_{uni}} = \frac{2\,v_s}{L_a} = 2560\ \mathrm{Hz} \tag{1}$$

where v_s is the satellite speed and L_a is the antenna length.

The intrinsic need to use two PRFs, one for each burst, leads to nonuniform azimuth sampling in at least one of the bursts. For these cases, a reconstruction algorithm has been implemented as described in [13]. Such nonuniform sampling typically leads to NESZ and azimuth ambiguity degradation; however, with proper PRF selection, these effects can be kept at acceptable levels. The criteria for the PRF selection are detailed in Section II-E.

Sections II-C–II-E unravel important aspects of the techniques that comprise the multiple-elevation-beam F-Scan with two-burst ScanSAR.

C. F-Scan and Variable PBW

The antenna front end considered assumes the availability of one PS and one true-time-delay line (TTDL) for each antenna element. The elements, in turn, are considered as ideal slotted waveguides with a wide sinc-like pattern. A uniform phase shift δ and time-delay difference $\Delta\tau$ between neighboring elements is assumed. These parameters can be calculated by

$$\delta = \frac{2\pi d}{c_0} \frac{(\sin\psi_\mathrm{f} - \sin\psi_\mathrm{n})}{\dfrac{1}{f_\mathrm{n}} - \dfrac{1}{f_\mathrm{f}}} \tag{2a}$$

$$\Delta\tau = \frac{d}{c_0}\left(\frac{f_\mathrm{f}\sin\psi_\mathrm{f} - f_\mathrm{n}\sin\psi_\mathrm{n}}{f_\mathrm{f} - f_\mathrm{n}}\right) \tag{2b}$$

where c_0 is the speed of light in free space, d is the element spacing, f is the transmit frequency, and ψ is the antenna off-boresight angle in elevation [21], [34]. Subscripts "f" and "n" refer to the farthest and the nearest pointings of the antenna at $t = 0$ and $t = t_\mathrm{p}$, respectively, with t_p being the pulse duration.

For such a configuration, the pointing angle for each frequency is given by

$$\psi = \arcsin\left[\frac{c_0}{d}\left(\Delta\tau - \frac{\delta}{2\pi f}\right)\right]. \tag{3}$$

A common approximation is to assume the pointing-by-frequency behavior as linear. However, for 1.2 GHz in X-band, there is a significant nonlinearity caused by the hyperbolic $1/f$ factor that needs to be considered. The main effect of this nonlinearity is a change in the distribution of the transmit frequencies across the scene, and thus a different estimation of the range resolution for each point on ground. An additional aspect to be considered as a consequence of the wide transmit bandwidth is the variation of the antenna pattern during the scanning. The half-power beamwidth (HPBW), for instance, varies about 12% both in elevation and in azimuth.

The common approach used in F-Scan to define when a target on ground has been fully imaged is the antenna HPBW. However, this definition is arbitrary, and one can for instance filter and process more or less than the −6 dB of the two-way power pattern. In this article, we propose processing a variable beamwidth as a function of the incidence angle with the intention of equalizing the ground range resolution. It can be an especially powerful tool at near range, where the slant-to-ground projection more significantly degrades the ground range resolution, and the backscatter is strong enough to afford a lower average antenna gain. The clear tradeoff of this technique is a higher effective bandwidth at the expense of a degraded noise performance. Assuming the antenna pattern correction and a Hamming window of $\alpha = 0.6$, Fig. 3 highlights this tradeoff for different power beamwidths (PBWs). It is shown by the two red marks, for instance, that a 52% increase in the bandwidth (and thus in resolution) can be achieved at the expense of 2 dB of NESZ. The Hamming window is responsible for strongly attenuating the stronger noise power increase from the antenna pattern correction. The selection of $\alpha = 0.6$ is also motivated by the actual value used by TerraSAR-X, which aims at having sidelobe suppression of at least 25 dB.

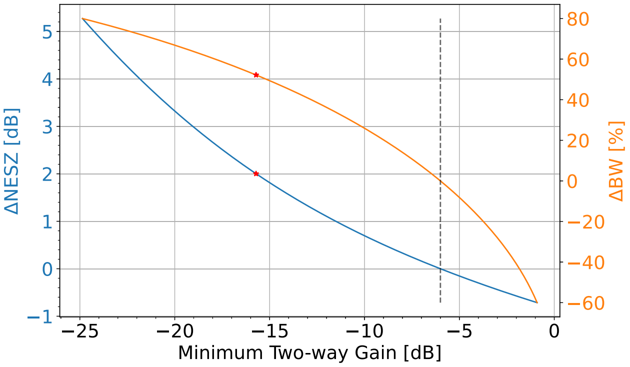

Fig. 3. Tradeoff between (right axis) effective bandwidth and (left axis) NESZ for different processed PBWs. The x-axis represents how much of the main lobe is processed. The reference is the typical −6 dB of the HPBW, and it is depicted by the vertical dashed line.

This technique is particularly useful in this context of ultra-wide imaging, as the variation of incidence angle is very relevant. However, it can be implemented in any sort of F-Scan acquisition. In summary, in order to precisely derive the effective bandwidth, average antenna gain, and echo timing for each target on ground, one needs to take into account: 1) the variable pattern in frequency; 2) the nonlinear scanning behavior; and 3) the variable processed PBW. In this research, this is done by simulations instead of analytical equations.

In [29], the equalization of both the ground range resolution and the azimuth resolution by means of using a down-chirp was discussed. For down-chirps, with respect to the nonlinear scanning curve, the linear approximation underestimates the bandwidth at far range and overestimates at near range. This effect happens because the antenna scans more slowly at higher frequencies than at lower ones. This behavior can be intuitively perceived by the frequency in the denominator of (3). The use of a down-chirp is still preferred as it equalizes the azimuth resolution, while the ground range resolution can be equalized by employing the aforementioned technique.

The possibility to process a variable amount of the main lobe combined with a fixed input ground range resolution creates an additional tradeoff. It is possible to use a lower transmit bandwidth and process more of the main lobe, and vice versa. The upper limit of this tradeoff is the maximum available transmit bandwidth, and the lower limit is the strong NESZ degradation due to the main lobe being very steep. Reducing the total transmit bandwidth for a fixed ground range resolution increases the illumination time of the targets, but at

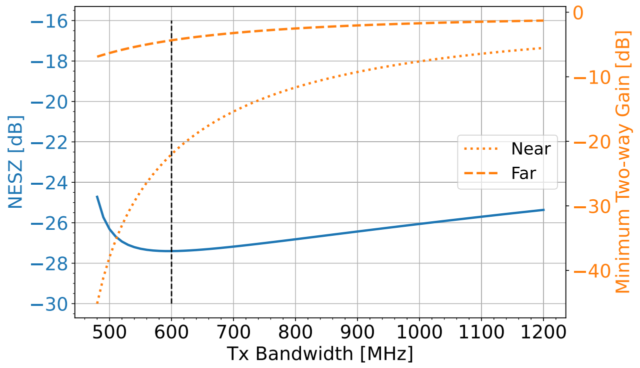

Fig. 4. Selection of the optimum transmit bandwidth based on NESZ minimization for a fixed ground range resolution of 10 m. The left axis depicts the average NESZ of the scene, while the right axis shows how much of the main lobe is processed at near and far range. The vertical dashed black line highlights the selected bandwidth of 600 MHz to minimize the average NESZ.

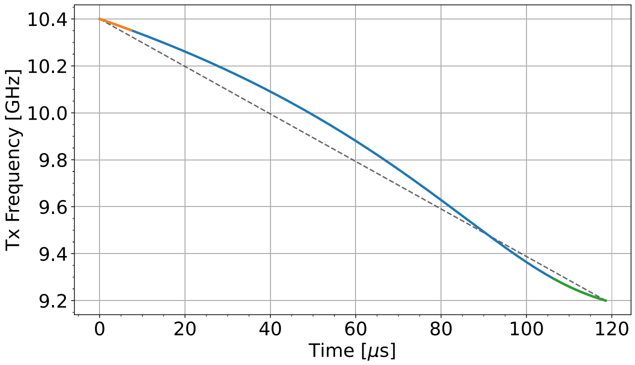

Fig. 5. Nonlinear chirp derived for an exemplary 300-km acquisition. The equivalent linear chirp is overlaid with the intention of highlighting the degree of nonlinearity. However, as each target is receiving only a fraction of the total bandwidth, the range spectrum of each target is still approximately rectangular. This fraction is highlighted for the far (in orange) and near (in green) targets.

the same time reduces the average antenna gain. The optimum point, i.e., the one that minimizes the NESZ, is used to determine the transmit bandwidth. Fig. 4 depicts this tradeoff and the selection of the optimum bandwidth of 600 MHz for an exemplary acquisition of a 300-km swath with 10-m resolution.

D. Nonlinear Chirp and Subpulses

The variable PBW introduced in Section II-C equalizes the ground range resolution by processing a larger portion of the main lobe. The resulting NESZ degradation at near range is considerably more significant than at far range. The degradation is compensated by transmitting a lower bandwidth and consequently achieving a longer illumination time for the same effective bandwidth. Both effects combined lead to a sort of equalization of the NESZ, i.e., it is improved at far and degraded at near range.

In order to achieve a full equalization of the NESZ, one can consider, for instance, scanning at a lower speed at far range, and faster at near range. Such a scanning speed variation allows for the tailoring of the illumination time, without influencing the bandwidth distribution. This adjustment is obtained by using a nonlinear transmit chirp whose frequency modulation (FM) rate varies in time to adjust the scanning speed according to a desired function.

The design of this nonlinear chirp starts by understanding that the dwell time (or illumination time, i.e., how long each target is illuminated by the processed part of the main lobe) increases for slower transmit frequency variations

$$t_d \propto \left| \frac{1}{\frac{d(f)}{dt}} \right|. \tag{4}$$

The dwell time for linear frequency-modulated (LFM) chirps, however, is a function of the incidence angle and not a constant value. Due to the one-to-one relation between angle and frequency in F-Scan, the dwell time can also be seen as a function of the frequency. Therefore, the dwell time for nonlinear chirps can be approximated as follows:

$$[t_d(f)]_{\mathrm{NL}} \approx k\,[t_{\mathrm{d}}(f)]_{\mathrm{LFM}}\,\frac{1}{\frac{df}{dt}} \tag{5}$$

where $[t_d(f)]_{\mathrm{LFM}}$ is the dwell time for an LFM chirp and k is a constant of proportionality. Finally, the time at which each frequency must be transmitted is given by

$$t(f) = \int_{f_{\mathrm{far}}}^{f} \frac{1}{k}\,\frac{[t_d(f)]_{\mathrm{NL}}}{[t_d(f)]_{\mathrm{LFM}}}\,df \tag{6}$$

with the boundary condition $t(f_{\mathrm{near}}) = t_{\mathrm{p}}$.

The next step is to determine what is the desired $[t_d(f)]_{\mathrm{NL}}$ to achieve an equalization of NESZ. This can be done by analyzing the NESZ equation and observing which parameters vary in range. To achieve a constant NESZ in range, it is required that

$$\frac{\lambda\, B_{\mathrm{eff}}\, R^3\, \sin\theta_{\mathrm{i}}\, \mathrm{APC}_{\mathrm{el}}}{t_d} = C \tag{7}$$

where λ is the wavelength, B_{eff} is the effective bandwidth, R is the slant range, θ_{i} is the incidence angle, $\mathrm{APC}_{\mathrm{el}}$ is the antenna pattern correction in elevation, and C is a constant. For an equalized ground range resolution, the product $B_{\mathrm{eff}} \sin\theta_{\mathrm{i}}$ is constant. Consequently, the behavior along the range of the desired dwell time for the nonlinear case is given by

$$[t_d(f)]_{\mathrm{NL}} \propto \lambda\, R^3\, \mathrm{APC}_{\mathrm{el}} \tag{8}$$

and thus, the nonlinear chirp is well-defined.

For visualization purposes, Figs. 5 and 6 depict the nonlinear chirp and the dwell time obtained for an exemplary acquisition of 300 km with 5-m resolution. Fig. 5 highlights in orange and green the fraction of the transmit pulse that is effectively received by the farthest and nearest targets. It shows that the degree of nonlinearity for the individual targets is, in general, much lower than that of the complete chirp.

The approach above is, to some extent, similar to the NBSR-T (nonlinear beam scanning response to time) introduced in [27]. The main differences arise from the fact that the approach in [27] is more abstract (generic polynomial

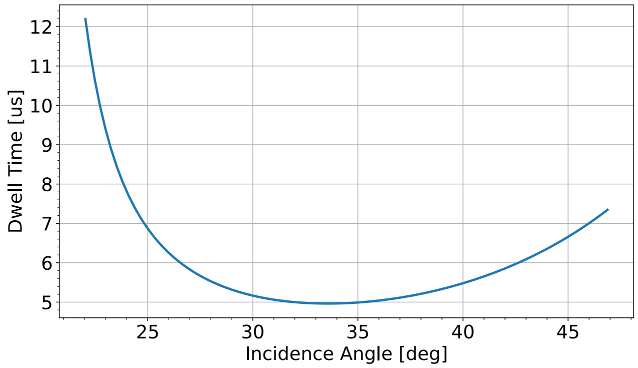

Fig. 6. Dwell time derived for an exemplary 300-km acquisition. The dwell time at near and far range is especially accentuated due to the higher effective bandwidth and the NESZ improvement needed, respectively.

scanning) and employs optimization methods to minimize the SNR difference between near and far range. Unfortunately, the formulation seems to disregard the backscatter variation from near to far range and thus corresponds to an equalization of the NESZ instead. The nonlinear waveform derived here is, in contrast, tailored specifically to NESZ equalization and takes into account the processing of a variable PBW and the Hamming window correction. In addition, due to the processing of a variable PBW (further discussion in Section III-C), the required level of nonlinearity of the chirp is not very strong and is reasonable even for swath widths of 300 km, as shown in Fig. 5.

As previously introduced, the transmit chirp can be divided into subpulses to improve the efficiency of the imaging. This is possible due to the existence of areas that do not contribute to the final image, namely, the blind ranges and the overlap between the subswaths of different bursts.

Skipping the transmission to the blind ranges is not straightforward. It is necessary to check if the imaging of the succeeding subswath has not yet started when the scanning of the previous one ended. For instance, if one would consider the illumination to be given by the HPBW, the angular extent of the blind range has to be larger than the HPBW to allow for skipping it. This issue tends to be more common at a far range, where the angular extent of the blind range is shorter.

An alternative way of visualizing this condition is by the concept of unused frequencies, i.e., those frequencies that are not used by either of the neighboring subswaths. The condition to skip a blind range is that there must be some unused frequencies, and the more there are, the more significant are the effects of skipping it. A visualization of the blind ranges and the unused frequencies for an exemplary acquisition is shown in Fig. 7.

Additional trimmings that can be done to the transmit pulse are with respect to, first, reducing the overlap between adjacent subswaths (considering both bursts) to around 1 km and, second, avoiding short subpulses when possible. This process must be done carefully taking into account the nadir interference and guaranteeing full imaging of the desired swath width.

After the transmit pulse is trimmed and separated into subpulses, the remaining individual transmit pulses are equally stretched in time to ensure the radar is transmitting continuously during its duty cycle. This step causes a small change in the timings of the echoes that must be considered, but that typically does not lead to an interfering scenario. Fig. 2 depicts the final time–frequency representation of the acquisition with subpulses.

E. ScanSAR and PRF Selection

Sections II-C and II-D described the relevant aspects of the novel mode in the range direction. This section, in turn, discusses the important design parameters in azimuth. The main points of attention are the design of the ScanSAR acquisition and the PRF selection.

The use of ScanSAR as a technique to eliminate the blind ranges has as its main consequence the degradation of the azimuth resolution. By employing two bursts, the resolution is effectively degraded by a factor of 3. Additionally, a nonhomogeneous amplitude modulation, known as the scalloping effect, appears in azimuth, as the targets are imaged by different portions of the azimuth antenna pattern.

The resolution and the scalloping effect are tightly related to the burst duration t_B. For the proposed mode, the burst duration represents how long the satellite is transmitting with each PRF. Longer burst durations typically result in better resolutions but also lead to worse scalloping and degraded azimuth ambiguity-to-signal ratio (AASR). It is directly linked to the target Doppler bandwidth by

$$B_\mathrm{D}^\mathrm{target}(\beta) = \frac{2\, v_\mathrm{r}^2}{\lambda\, R}\, t_\mathrm{B} \tag{9}$$

where v_r is the effective speed and β in parenthesis highlights the dependency on the look angle. The azimuth resolution requirement, in turn, can also be related to the Doppler bandwidth by

$$B_\mathrm{D}^\mathrm{target}(\beta) \geq \frac{0.886\, v_\mathrm{g}\, \gamma_\mathrm{w,az}}{\delta_\mathrm{az}^\mathrm{worst}} \tag{10}$$

where v_g is the ground speed, $\gamma_\mathrm{w,az}$ is the broadening factor of the Hamming window in azimuth, and $\delta_\mathrm{az}^\mathrm{worst}$ is the worst case azimuth resolution in the scene. Finally, in order to satisfy the minimum resolution requirement, the burst duration is derived by

$$t_\mathrm{B} \geq \frac{0.886\, \gamma_\mathrm{w,az}}{2\, v_\mathrm{s}\, \delta_\mathrm{az}^\mathrm{worst}}\, \max_{\beta}(\lambda\, R) \tag{11}$$

where the minimum allowed value is assumed to avoid worsening both AASR and scalloping. By transmitting shorter wavelengths to far range, i.e., by using down-chirps, the term $\max_\beta(\lambda\, R)$ can be reduced, thus also reducing the burst duration and the scalloping effect. In addition, a down-chirp also equalizes the target Doppler bandwidth in (9), thus equalizing the performance in azimuth across range.

The selection of an adequate PRF for each acquisition is an essential step. For the proposed mode, the design of the PRFs for each burst takes into account several factors. First, the PRFs must lead to different blind range positions such that there is no overlap between the gaps, thus guaranteeing

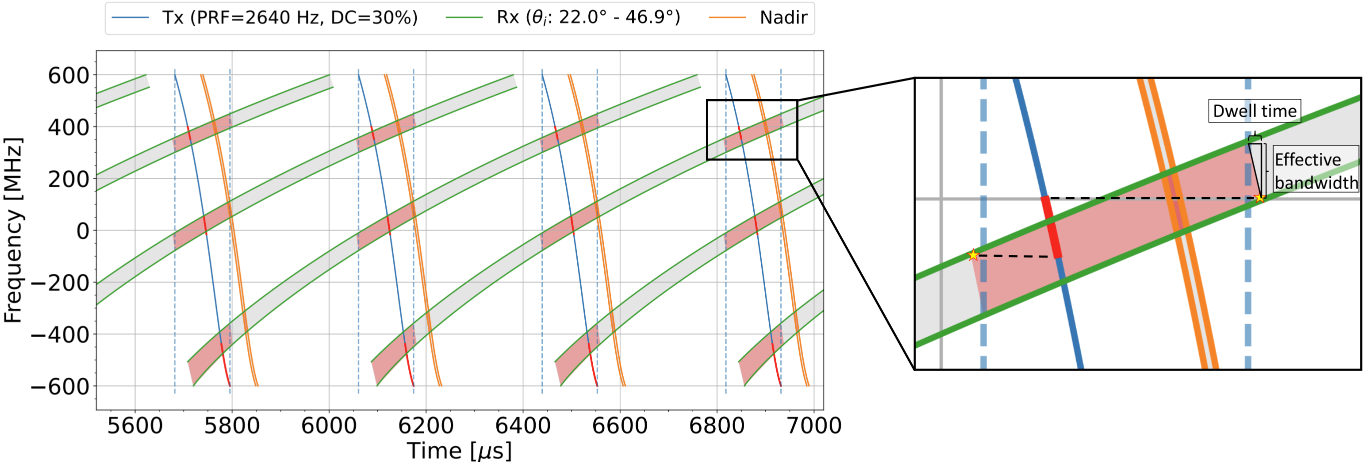

Fig. 7. Visualization of the transmit and receive events highlighting the blind ranges and the unused frequencies. The parts of the transmit pulses with frequencies that do not appear in any subswath are in red. Similarly, the parts of the echoes that are lost due to transmit and nadir interference are filled in light red. On the right side, the derivation of the unused frequency interval is depicted. The stars highlight the minimum/maximum frequencies of the imaged subswaths (in gray). Additionally, the dwell time and the effective bandwidth of the target at the interface between the imaged and blind areas are shown.

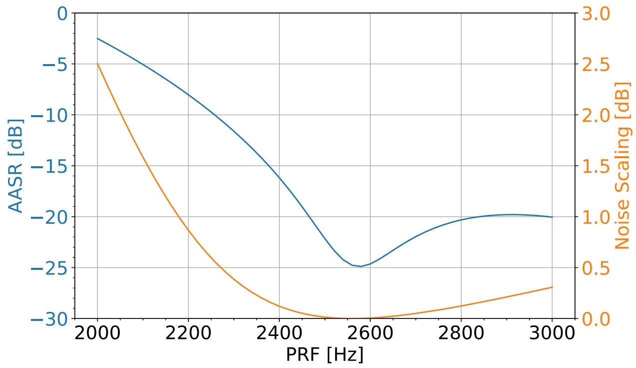

Fig. 8. AASR and noise scaling from the multichannel reconstruction as a function of the PRF for a two-burst ScanSAR acquisition with 300-km swath width, 5-m azimuth resolution, and a Hamming window of $\alpha = 0.6$.

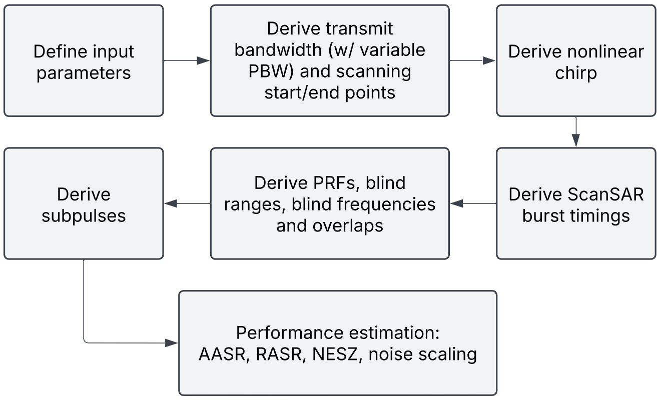

Fig. 9. Flowchart summarizing the design steps for a multiple-elevation-beam F-Scan with two-burst ScanSAR acquisition.

that the final image is contiguous. Second, the combination of the PRF and the number of azimuth channels must be sufficient to ensure an adequate sampling, which is required for good AASR levels and for the target resolution to be achieved. Finally, the PRF still needs to respect the DPCA reconstruction requirements, i.e., highly nonuniform sampling must be avoided, as it leads to strong noise scaling and AASR degradation.

The procedure adopted here is to first understand the AASR and noise scaling variation as a function of the PRF. This behavior is depicted in Fig. 8, where it becomes evident that the best solutions performance-wise are PRFs around the uniform sampling case (a PRF of 2560 Hz) derived in (1). The PRF range is then investigated in the vicinity of the uniform sampling case for pairs of PRFs that respect the timing constraints, i.e., those PRFs that do not lead to an overlap between the blind ranges for the desired scene. Finally, these pairs of PRFs are individually evaluated in terms of AASR, and the one with the best worst case AASR is selected. A more thorough analysis of the AASR is found in Section III-A.

F. Summary of the Mode Design

The most relevant techniques and concepts necessary for the understanding of the proposed mode have been described in this section. It becomes clear that it involves the concatenation of multiple techniques. Therefore, the design of an acquisition for such a mode can potentially follow multiple paths. The techniques in this section are presented in the given order for the sake of clarity. However, the exact procedure taken in the simulation algorithm is summarized in Fig. 9.

III. PERFORMANCE ASSESSMENT

Section II introduced the novel mode and described in detail the design of the acquisition parameters. In this section, the estimation of relevant performance figures is explained.

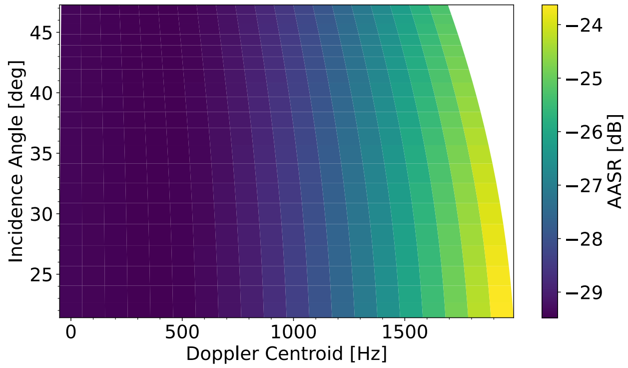

Fig. 10. AASR as a function of the incidence angle and the Doppler centroid for an acquisition with a swath width of 300 km, an azimuth resolution of 5 m, a Hamming window of $\alpha = 0.6$, and a PRF of 2640 Hz.

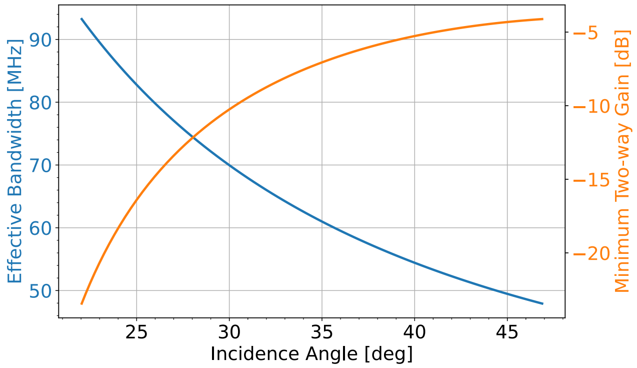

Fig. 11. Effective bandwidth and the respective minimum two-way gain as a function of the incidence angle for a 300-km acquisition with a constant 5-m ground range resolution and a transmit bandwidth of 1200 MHz.

A. Azimuth Performance

The main performance parameters of interest in azimuth are the resolution, the scalloping, and the ambiguity-to-signal ratio. These parameters vary significantly in the range direction due to the fixed burst duration, accompanied by the high variation in wavelength and slant range. This behavior can already be recognized in (9) and was briefly discussed in Section II-E. For the wide scenes considered in this research, the slant range variation is more significant than the maximum wavelength variation. Therefore, the available bandwidth is the lowest at far range, and it dictates the best achievable azimuth resolution. In order to obtain a constant azimuth resolution, the processed bandwidth for every range position is assumed to be equal to this minimum bandwidth.

For exemplification, a 300-km swath width with a 5-m resolution would lead to a burst duration of 0.32 s, a target Doppler bandwidth varying from 1657 to 1935 Hz (being the total Doppler bandwidth three times larger) and a scalloping effect varying from 0.8 to 1.1 dB (far to near).

Finally, the azimuth ambiguity performance is also a very relevant image quality parameter. Details on the derivation of AASR and noise scaling for a multichannel system operating in burst mode can be found in [35]. For the system and mode considered, the AASR variation with PRF was highlighted in Fig. 8. The figure highlights the worst case AASR in the scene for different PRFs, i.e., it represents the AASR at near range for the target with the highest Doppler centroid (at the edge of the main lobe, strongest scalloping). Nevertheless, for the remaining of the scene, the AASR has significantly better values. For the same scenario of a swath width of 300 km and 5-m resolution, Fig. 10 depicts the AASR variation across the whole scene for a PRF of 2640 Hz. It becomes clear that, although the worst case is −23.6 dB, the majority of the scene depicts an even better performance with a best case of about −29.5 dB. The PRF of the other burst—2530 Hz—has slightly better AASR performance and shows a similar behavior over incidence angle and Doppler centroid.

Finally, improving the azimuth resolution by means of increasing the burst duration would lead to strong tradeoffs in terms of scalloping effect and mainly AASR. For instance, improving the resolution from 5 to 4 m and 3 m would degrade the worst case AASR from −23.6 to −19.2 dB and −12.0 dB, respectively, and scalloping would increase from 1.1 to 1.8 dB and 3.3 dB. Therefore, for the sake of preserving image quality, a maximum resolution of 5 m is adopted.

B. Range Performance

Similarly, in range, the main performance parameters of interest are the resolution and the ambiguity-to-signal ratio. As introduced in Section II-C, the ground range resolution can be totally equalized—even for ultra-wide scenes—by receiving and processing a variable PBW, given that the desired resolution is not too aggressive (too fine). For this purpose, the required effective bandwidth in the range can be derived by

$$B_{\mathrm{eff}}(\theta_{\mathrm{i}}) = \frac{0.886\, c_0\, \gamma_{\mathrm{w,rg}}}{2\, \delta_{\mathrm{gr}}\, \sin\theta_{\mathrm{i}}} \tag{12}$$

where $\gamma_{\mathrm{w},rg}$ is the broadening factor of the Hamming window in range and δ_{gr} is the desired ground range resolution. For an exemplary acquisition, Fig. 11 depicts on the left axis the variation of the effective bandwidth along range and on the right axis how much of the main lobe is processed. The need for a higher effective bandwidth at near range is a direct consequence of the slant-to-ground projection factor represented by the sine of the incidence angle in (12).

The ambiguities in range for F-Scan systems tend not to be an important concern. The employment of a high-gain pencil beam leads to strong attenuation of the ambiguous regions. Consequently, the range ambiguity-to-signal ratio (RASR) is typically very low. In addition, due to the antenna scan, the target and ambiguities average gains vary much less than in traditional acquisitions with static antennas, thus leading to a relatively smooth RASR curve. Considering the approach introduced in [36, eqs. (15) and (16)], the RASR for the aforementioned example is depicted in Fig. 12.

Despite the clear and expected tendency of worse RASR for higher incidence angles, the RASR is still at excellent levels, being below about −41 dB. For the system considered, RASR becomes an issue for incidence angles higher than about 60°, mainly due to the appearance of grating lobes. Therefore, such high incidence angles are disregarded in this research.

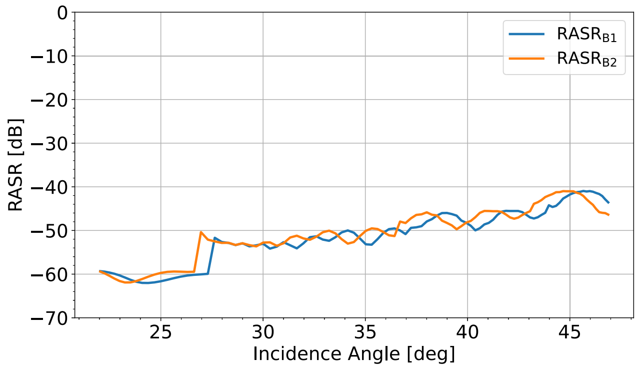

Fig. 12. RASR of bursts 1 and 2 as a function of the incidence angle for an acquisition of 300 km with a resolution of 5 m.

C. Noise-Equivalent Sigma-Zero

An additional key parameter for describing the image quality is the NESZ. It is especially relevant in this work, as essentially every technique considered affects it. The objective, as shown previously in this article, is to keep it as low and uniform as possible throughout the scene. The influence of each technique is summarized next and subsequently plots highlighting the improvements are provided.

The use of F-Scan has three main effects. First, the scanning leads to the effect that targets in range have a similar average gain. For traditional F-Scan acquisitions with swaths of about 50 km, the NESZ is then almost flat as can be seen in [24, Fig. 13]. This is a beneficial result when compared to the high NESZ variation in traditional Stripmap acquisitions. Second, the use of high-gain pencil beams clearly increases the average gain of the targets, being also a beneficial effect. Finally, a detrimental characteristic is the fact that due to the scanning, each target is illuminated for only a fraction of the transmit pulse, consequently degrading the NESZ.

Next, the processing of a variable PBW to equalize the ground range resolution leads, on the one hand, to a clear deterioration of the NESZ at near range, as much more than the typical −6 dB of the HPBW is considered. On the other hand, a lower transmit bandwidth can be used for the same target resolution, thus improving the NESZ. In addition, if processing only the HPBW, the minimum near-range incidence angle is predefined for a given input swath width and worst case ground range resolution. Consequently, when aiming at better resolutions and wider swaths, the incidence angle range of the swath may be nonoptimal. For instance, 300 km at 5-m resolution would require an incidence angle range from 32° to 53°. The implementation of the variable PBW technique allows for a more interesting range (in terms of NESZ and ambiguities); in this case, from 22° to 47°, this also has a very positive impact on the final NESZ.

Concerning the use of a nonlinear chirp, it was envisaged exactly to equalize the NESZ by better distributing the transmitted energy across the scene. This is especially helpful for the ultra-wide scenes considered here, as there is a huge variation in distance between satellite and near and far range. This redistribution of energy tends to improve the NESZ at far range and degrade it at near range, guaranteeing in the end a homogeneous NESZ and a strongly improved worst case. Similar to traditional Stripmap imaging, there will be a variation in intensity across range in the focused image. This effect must be taken into account during processing and calibration to get the proper brightness profile in range.

In comparison, dividing the transmit pulse into subpulses is not a matter of redistribution, but of a more efficient distribution of energy, leading to real NESZ gains for the whole scene.

Finally, the use of ScanSAR has as its main consequence the different azimuth gains known as the scalloping effect. Nevertheless, the final worst case NESZ can still be kept at excellent levels for the mode proposed.

The theoretical derivation of the NESZ takes into account all the factors described above. The final equation is given by (13) shown at the bottom of the page, where P_t is the peak transmit power, l is the antenna length of each azimuth channel, h is the antenna height, k_{B} is Boltzmann's constant, $T = 290$ K is a reference temperature, F is the system noise figure, L is the system losses, N_{DPCA} is the number of azimuth channels, W is the Hamming window, $C_{\mathrm{el/az}}$ is the antenna field patterns in elevation and azimuth, f_{D} is the Doppler frequency, and $B_{\mathrm{D}}, \mathrm{p}$ is the processed Doppler bandwidth.

In order to visualize the improvements brought by each technique, as well as to highlight the NESZ levels expected for the mode, Fig. 13 depicts the NESZ for a 300 km acquisition with a ground range resolution lower than 5 m.

Initially, Fig. 13(a) portrays the NESZ curve for the proposed mode at its most basic version, i.e., with multiple-elevation-beam F-Scan and ScanSAR only. As a first improvement step, Fig. 13(b) highlights the NESZ deterioration at near range, improvement at far range, and, most importantly, the better incidence angle range that can be used as a consequence of processing a variable PBW. Subsequently, Fig. 13(c) demonstrates the equalized NESZ achieved by employing the nonlinear chirp previously derived. Finally, Fig. 13(d) presents the scene-wide improvements brought by the use of subpulses. Overall, a substantial improvement of 6.3 dB in the worst case NESZ is achieved between the optimized mode and its basic concept.

D. Performance Summary

This section summarizes the main image quality parameters of interest for different scenarios considering the mode optimized with the techniques introduced in this article and the

$$\mathrm{NESZ} = \frac{16\pi\lambda}{P_t l^2 h^2}\,\frac{k_{\mathrm{B}} T B_{\mathrm{eff}} F L}{c_0 N_{\mathrm{DPCA}}}\,\frac{v_{\mathrm{s}} R^3 \sin\theta_{\mathrm{i}}}{t_d \mathrm{PRF}}\,\frac{\int_{B_{\mathrm{eff}}} \frac{W^2(f)}{|C_{\mathrm{el}}(f,\beta)|^4}\,\mathrm{d}f}{\int_{B_{\mathrm{eff}}} W^2(f)\,\mathrm{d}f}\,\frac{\int_{B_{\mathrm{D,p}}} \frac{W^2(f_{\mathrm{D}})}{|C_{\mathrm{az}}(f_{\mathrm{D}})|^4}\,\mathrm{d}f_{\mathrm{D}}}{\int_{B_{\mathrm{D,p}}} W^2(f_{\mathrm{D}})\,\mathrm{d}f_{\mathrm{D}}}. \tag{13}$$

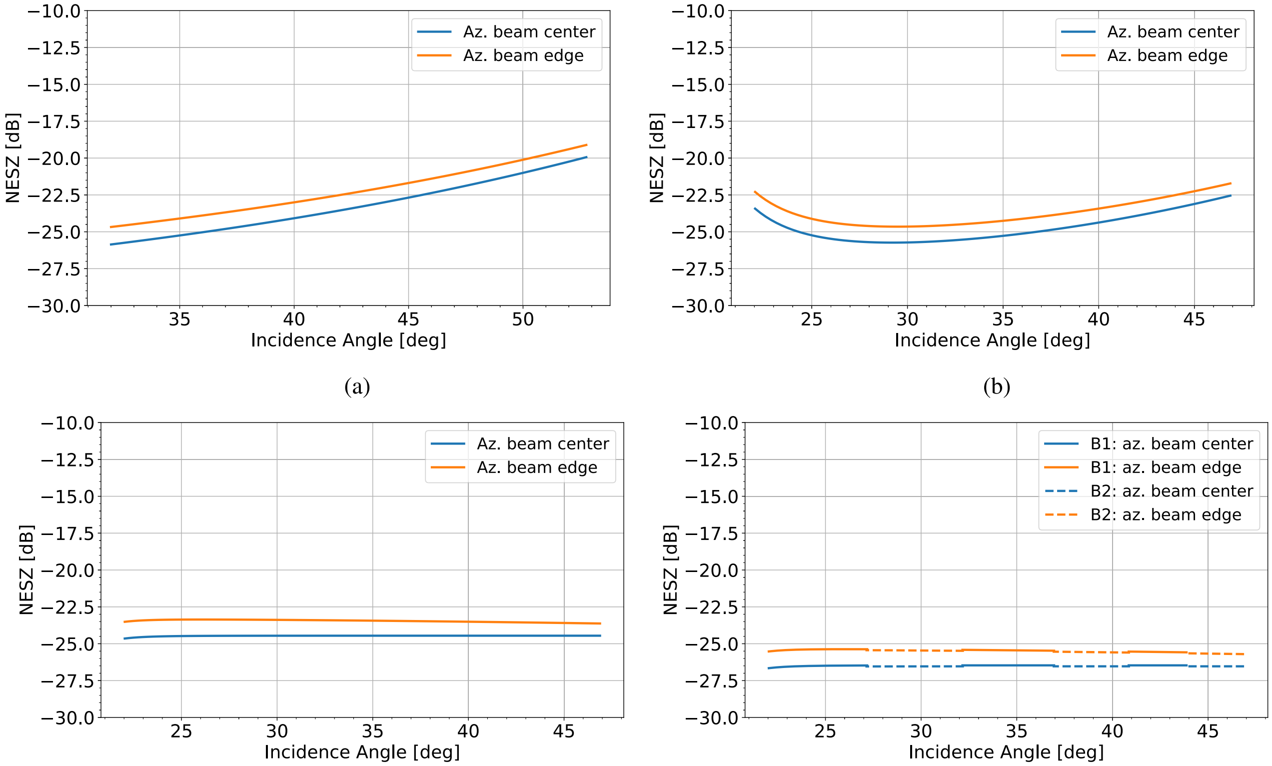

(a) (b)

(c) (d)

Fig. 13. NESZ curves for a 300-km acquisition with a ground range resolution of 5 m or lower. The improvements brought by each of the proposed techniques are highlighted. A very significant improvement in the image quality is achieved at the cost of a modest increase in the complexity of the acquisition and of the processing. The curves for each burst are merged in (a)–(c) because they are identical. (a) Original NESZ (<−19.1 dB). (b) NESZ w/ variable PBW (<−21.7 dB). (c) NESZ w/ variable PBW and nonlinear chirp (<−23.3 dB). (d) NESZ w/ variable PBW, nonlinear chirp, and subpulses (<−25.4 dB).

TABLE II

PERFORMANCE SUMMARY OF THE PROPOSED MODE FOR DIFFERENT INPUT SWATH WIDTH AND RESOLUTION REQUIREMENTS CONSIDERING THE SYSTEM PARAMETERS IN TABLE I

#	Inc. angle	Tx BW	Swath width	PRFs	Az. res.	Gr. res.	NESZ	AASR	RASR
1	22°-40°	1180 MHz	200 km	2540 Hz / 2650 Hz	4 m	4 m	< -26.2 dB	< -21.4 dB	< -45.9 dB
2	21°-39°	990 MHz	200 km	2520 Hz / 2650 Hz	5 m	5 m	< -27.7 dB	< -24.2 dB	< -45.9 dB
3	22°-47°	1200 MHz	300 km	2530 Hz / 2640 Hz	5 m	5 m	< -25.4 dB	< -23.6 dB	< -40.9 dB
4	24°-54°	1200 MHz	400 km	2530 Hz / 2640 Hz	5 m	5 m	< -22.7 dB	< -21.9 dB	< -35.3 dB
5	20°-57°	1200 MHz	500 km	2530 Hz / 2630 Hz	7 m	7 m	< -23.3 dB	< -25.8 dB	< -33.0 dB
6	20°-57°	850 MHz	500 km	2530 Hz / 2630 Hz	10 m	10 m	< -25.5 dB	< -28.4 dB	< -33.0 dB

parameters shown in Table I. For varying input requirements of swath width and resolution, the main acquisition and performance parameters are derived and displayed in Table II. The results obtained highlight the very high image quality coupled with ultra-wide-swath width that can be achieved with a system endowed with F-Scan capabilities and multiple channels in azimuth, similar to the mission proposal HRWS.

The derivation of the parameters listed in Table II follows the explanations given in Sections III-A–III-C. The incidence angle ranges were manually optimized for the specific platform height and system parameters to yield better performance.

Comparing the PRF pairs obtained with the exemplary curve for AASR and noise scaling shown in Fig. 8, two interesting observations can be made. First, the lower PRF needs to be closer to the uniform sampling case, as the AASR deterioration is steeper for PRFs just below 2560 Hz compared to those above it. Second, the noise scaling is clearly not an issue, as it is mostly below 0.05 dB for the PRF pairs selected. As the noise scaling is negligible compared to the achieved NESZ, this parameter has been omitted from Table II to preserve readability.

On the one hand, as expected and previously discussed, the RASR for all the examples is also not an issue due to the large antenna height. The AASR, on the other hand, shows a clear tradeoff at higher incidence angles and enhanced azimuth resolutions, where a larger burst duration is needed. Similarly, the NESZ also shows some degradation at higher incidence angles and transmit bandwidths. The examples are designed in a way that the final performance is at very good levels for all the parameters.

Overall, all the examples depict large swaths with great imaging performance. Nevertheless, scenario 4 shows a good compromise between all the parameters, being a good candidate for large-scale imaging.

IV. DISCUSSION AND FURTHER WORK

The technique introduced here is one alternative to achieve ultra-wide swaths with an F-Scan system. A more conventional approach would be to perform a simple ScanSAR acquisition with many bursts. It is interesting to understand the differences between these two techniques. First, the approach presented in this article employs only two bursts, but scans over a very wide swath. Hence, the range resolution is more strongly degraded, but the azimuth resolution is not so much. As a consequence, for the system under analysis, the final 2-D resolution is properly balanced between the two main directions. In contrast, a conventional ScanSAR would have shorter scans in elevation but would require a much larger number of bursts. Thus, the resolution would be highly unbalanced between azimuth and range, being very good in range, but highly degraded in azimuth. This unbalanced resolution is observed in the present X-band SAR systems like TerraSAR-X, COSMO-SkyMed SG, and ICEYE [3], [4], [5].

Another possibility with this mode is to include one or two additional bursts. For instance, a three-burst case would have an additional gapless swath at near range. Keeping the same total swath width, this approach would degrade performance in azimuth due to the extra burst but improve the NESZ, as lower transmit bandwidths could be used to achieve the same ground range resolution. However, as can be observed in Table II, this tradeoff is not strictly necessary, and the mode would have even more additional complexity.

Depending on the mission objectives, if one would prioritize resolution over swath width, it would be possible to also save some costs by reducing the antenna height. Clearly, the NESZ would be degraded, but still good levels could be potentially achieved for a 3-m case with maybe 200- or 300-km swaths.

For future work, a topic of interest would be to analyze the processing window to be used in the range. In this investigation, a conventional Hamming window with $\alpha = 0.6$ was considered. However, due to the processing beyond the HPBW, one could consider a more aggressive window to get a stronger attenuation of the noise power increase caused by the antenna pattern correction.

Additionally, another topic worth of further investigation is a detailed analysis of the exact phase spoiling needed in azimuth on transmit. Potentially, the 12 antenna elements in azimuth may not be enough to achieve a nice spoiled pattern, thus leading to either some performance degradation or the need for more elements.

The concept and performance prediction of this innovative mode have been described in this article. Nevertheless, the exact processing steps, optimizations, and topography considerations must be topics for future investigation, in case this mode is actually considered for a real implementation. To further analyze and visualize the performance of the new imaging mode presented in this article, it would be useful to implement a full end-to-end SAR system simulator that can cover the entire swath width for realistic scenarios with topography and distributed scatterers.

Besides, it would also be expected to consider replacing ScanSAR by TOPS to get a more uniform performance in azimuth. However, as shown in Fig. 13, the scalloping effect is only about 1 dB so that the additional complexity introduced by TOPS may not be advantageous. Alternatively, one could also opt for PRI variation approaches rather than ScanSAR as a way to overcome the blind ranges, thus avoiding the azimuth resolution deterioration, but raising additional challenges and complexity.

Finally, the analysis presented in this article assumes ideal hardware conditions and ignores channel imbalances. A dedicated calibration procedure for F-Scan is needed to take into account the potentially frequency-dependent behavior of the amplitude and phase imbalances. Such an investigation is topic of future work and would be valuable not only for the mode introduced in this article but also for any F-Scan imaging approach. Some research on the calibration of wideband SAR systems has already been published and can be of advantage in the F-Scan specific analysis [37].

V. CONCLUSION

The multiple-elevation-beam F-Scan with two-burst ScanSAR is shown to be a powerful technique capable of achieving ultra-wide swaths with very good imaging performance. It represents an interesting alternative to more complex techniques employing fully fledged DBF approaches, such as SCORE. The main novelty that makes this mode possible is a new method of using F-Scan, i.e., simultaneously receiving otherwise ambiguous swaths and differentiating them in the space–frequency domain by the intrinsic beamsteering of F-Scan. The novel mode expands the already existing very high-resolution imaging capabilities of an HRWS-like system to also be able to obtain ultra-wide swaths in X-band without strongly compromising the azimuth resolution.

This article provided an in-depth description of the concept, the techniques involved, and the performance estimation of the novel mode. It stands out as an imaging technique capable of achieving very high and homogeneous performance, without prioritizing one direction over the other. Both the NESZ and the ground range resolution are shown to be fully equalized across range by exploiting the flexibility of F-Scan. Finally, a very significant improvement of the worst case NESZ was also achieved. For instance, for scenario 3 in Table II, it was shown that a considerable improvement of 6.3 dB can be obtained with the proposed techniques.

ACKNOWLEDGMENT

The authors would like to express their appreciation to the anonymous reviewers for their insightful feedback, which significantly enhanced the quality of the article.

REFERENCES

[1] A. Moreira, P. Prats-Iraola, M. Younis, G. Krieger, I. Hajnsek, and K. P. Papathanassiou, "A tutorial on synthetic aperture radar," *IEEE Geosci. Remote Sens. Mag.*, vol. 1, no. 1, pp. 6–43, Mar. 2013.

[2] J. C. Yoon et al., "KOMPSAT-5 SAR design and performance," in *Proc. 3rd Int. Asia–Pacific Conf. Synth. Aperture Radar (APSAR)*, Sep. 2011, pp. 1–4.

[3] M. Eineder et al. (2013). *TerraSAR-X Basic Product Specification Document*. [Online]. Available: https://sss.terrasar-x.dlr.de/docs/TX-GS-DD-3302.pdf

[4] (2021). *COSMO-SkyMed Seconda Generazione: System and Products Description*. [Online]. Available: https://earth.esa.int/eogateway/documents/20142/37627/COSMO-SkyMed-Second-Generation-Mission-Products-Description.pdf

[5] V. Ignatenko, M. Nottingham, A. Radius, L. Lamentowski, and D. Muff, "ICEYE microsatellite SAR constellation status update: Long dwell spotlight and wide swath imaging modes," in *Proc. IEEE Int. Geosci. Remote Sens. Symp.*, Jul. 2021, pp. 1493–1496.

[6] A. Moreira, M. Zink, M. Bartusch, A. E. Nuncio Quiroz, and S. Stettner, "German spaceborne SAR missions," in *Proc. IEEE Radar Conf. (RadarConf)*, May 2021, pp. 1–6.

[7] J. Mittermayer et al., "MirrorSAR: An HRWS add-on for single-pass multi-baseline SAR interferometry," *IEEE Trans. Geosci. Remote Sens.*, vol. 60, 2022, Art. no. 5224018.

[8] D. Geudtner, R. Torres, P. Snoeij, M. Davidson, and B. Rommen, "Sentinel-1 system capabilities and applications," in *Proc. IEEE Geosci. Remote Sens. Symp.*, Jul. 2014, pp. 1457–1460.

[9] R. Torres et al., "Sentinel-1 next generation: Enhanced C-band data continuity," in *Proc. 14th Eur. Conf. Synth. Aperture Radar*, Jul. 2022, pp. 1–3.

[10] A. Currie and M. A. Brown, "Wide-swath SAR," *IEE*, vol. 139, no. 2, p. 122, 1992.

[11] M. Suess, B. Grafmueller, and R. Zahn, "A novel high resolution, wide swath SAR system," in *Proc. IEEE Int. Geosci. Remote Sens. Symp. (IGARSS)*, Jul. 2001, pp. 1013–1015.

[12] M. Suess and W. Wiesback, *Side-looking synthetic aperture radar system*, EP Patent 1 241 487 B1, Sep. 18, 2002.

[13] G. Krieger, N. Gebert, and A. Moreira, "Unambiguous SAR signal reconstruction from nonuniform displaced phase center sampling," *IEEE Geosci. Remote Sens. Lett.*, vol. 1, no. 4, pp. 260–264, Oct. 2004.

[14] G. Krieger, N. Gebert, and A. Moreira, "Multidimensional waveform encoding: A new digital beamforming technique for synthetic aperture radar remote sensing," *IEEE Trans. Geosci. Remote Sens.*, vol. 46, no. 1, pp. 31–46, Jan. 2008.

[15] G. Krieger, N. Gebert, M. Younis, F. Bordoni, A. Patyuchenko, and A. Moreira, "Advanced concepts for ultra-wide-swath SAR imaging," in *Proc. 7th Eur. Conf. Synth. Aperture Radar*, Jun. 2008, pp. 1–4.

[16] G. Krieger, N. Gebert, M. Younis, and A. Moreira, "Advanced synthetic aperture radar based on digital beamforming and waveform diversity," in *Proc. IEEE Radar Conf.*, May 2008, pp. 1–6.

[17] N. Gebert and G. Krieger, "Ultra-wide swath SAR imaging with continuous PRF variation," in *Proc. 8th Eur. Conf. Synth. Aperture Radar*, Jun. 2010, pp. 1–4.

[18] A. Freeman et al., "SweepSAR: Beam-forming on receive using a reflector-phased array feed combination for spaceborne SAR," in *Proc. IEEE Radar Conf.*, May 2009, pp. 1–9.

[19] M. Villano, G. Krieger, and A. Moreira, "Staggered SAR: high-resolution wide-swath imaging by continuous PRI variation," *IEEE Trans. Geosci. Remote Sens.*, vol. 52, no. 7, pp. 4462–4479, Jul. 2014.

[20] F. Q. de Almeida, M. Younis, P. Prats-Iraola, M. Rodriguez-Cassola, G. Krieger, and A. Moreira, "Slow pulse repetition interval variation for high-resolution wide-swath SAR imaging," *IEEE Trans. Geosci. Remote Sens.*, vol. 59, no. 7, pp. 5665–5686, Jul. 2021.

[21] C. Roemer, "Introduction to a new wide area SAR mode using the F-SCAN principle," in *Proc. IEEE Int. Geosci. Remote Sens. Symp. (IGARSS)*, Jul. 2017, pp. 3844–3847.

[22] C. Roemer, *High resolution wide swath synthetic aperture system*, WO Patent 2 019 015 911 A1, Jan. 24, 2019.

[23] L. Nan, G. Gai, T. Shiyang, and Z. Linrang, "Signal modeling and analysis for elevation frequency scanning HRWS SAR," *IEEE Trans. Geosci. Remote Sens.*, vol. 58, no. 9, pp. 6434–6450, Sep. 2020.

[24] M. Younis, F. Q. de Almeida, T. Bollian, M. Villano, G. Krieger, and A. Moreira, "A synthetic aperture radar imaging mode utilizing frequency scan for time-of-echo compression," *IEEE Trans. Geosci. Remote Sens.*, vol. 60, 2022, Art. no. 5239917.

[25] P. Guccione, D. Mapelli, D. Giudici, and A. R. Persico, "Design of f-SCAN acquisition mode for synthetic aperture radar," *Remote Sens.*, vol. 14, no. 20, p. 5283, Oct. 2022.

[26] N. Gollin, R. Scheiber, M. Martone, P. Rizzoli, and G. Krieger, "SAR imaging in frequency scan mode: System optimization and potentials for data volume reduction," *IEEE Trans. Geosci. Remote Sens.*, vol. 61, 2023, Art. no. 5200420.

[27] B. Li, D. Liang, Y. Nan, J. Li, P. Lu, and R. Wang, "A novel nonlinear frequency scanning SAR imaging mode," *IEEE Trans. Geosci. Remote Sens.*, vol. 62, 2024, Art. no. 5220424.

[28] J. P. T. Ribeiro, T. Kraus, M. Bachmann, A. Moreira, and G. Krieger, *Synthetik-apertur-radarverfahren*, German Patent 1 020 231 130 293, Nov. 21, 2024.

[29] J. P. T. Ribeiro, G. Krieger, T. Kraus, M. Bachmann, and A. Moreira, "Spaceborne multiple-swath SAR imaging with frequency scanning," in *Proc. EUSAR*, 2024, pp. 697–702.

[30] F. Bordoni, M. Younis, and G. Krieger, "Performance investigation on the high-resolution wide-swath SAR system operating in multisubpulse mode," in *Proc. IEEE Int. Geosci. Remote Sens. Symp.*, Jul. 2012, pp. 3568–3571.

[31] F. Bordoni, G. Krieger, and M. Younis, "Multifrequency subpulse SAR: Exploiting chirp bandwidth for an increased coverage," *IEEE Geosci. Remote Sens. Lett.*, vol. 16, no. 1, pp. 40–44, Jan. 2019.

[32] M. Bartusch, C. Bruens, A. E. Nuncio Quiroz, and S. Stettner, "HRWS: The upcoming German X-band spaceborne SAR mission," in *Proc. 13th Eur. Conf. Synth. Aperture Radar*, Mar. 2021, pp. 1–4.

[33] M. Villano, G. Krieger, and A. Moreira, "Advanced spaceborne SAR systems with planar antenna," in *Proc. IEEE Radar Conf. (RadarConf)*, May 2017, pp. 0152–0156.

[34] C. A. Balanis, *Antenna Theory: Analysis and Design*, 4th ed., Hoboken, NJ, USA: Wiley, 2016.

[35] N. Gebert, G. Krieger, and A. Moreira, "Multichannel azimuth processing in ScanSAR and TOPS mode operation," *IEEE Trans. Geosci. Remote Sens.*, vol. 48, no. 7, pp. 2994–3008, Jul. 2010.

[36] J. P. T. Ribeiro, T. Kraus, M. Bachmann, R. Machado, G. Krieger, and A. Moreira, "Concurrent SAR imaging with F-scan: Timing design and performance prediction," *IEEE Trans. Geosci. Remote Sens.*, vol. 62, 2024, Art. no. 5218217.

[37] X. Wang et al., "Precise calibration of channel imbalance for very high resolution SAR with stepped frequency," *IEEE Trans. Geosci. Remote Sens.*, vol. 55, no. 8, pp. 4252–4261, Aug. 2017.